frontiers in Earth Science

ORIGINAL RESEARCH
published: 26 November 2019
doi: 10.3389/feart.2019.00306

Neutron Imaging of Cadmium Sorption and Transport in Porous Rocks

Benoît Cordonnier[1], Anne Pluymakers[2], Alessandro Tengattini[3,4], Sina Marti[5], Anders Kaestner[6], Florian Fusseis[5] and François Renard[1,7]*

[1] Departments of Geosciences and Physics, The Njord Centre, Physics of Geological Processes, University of Oslo, Oslo, Norway, [2] Department of Geoscience and Engineering, Faculty of Civil Engineering and Geosciences, TU Delft, Delft, Netherlands, [3] Univ. Grenoble Alpes, CNRS, Grenoble INP, 3SR, Grenoble, France, [4] Institute Laue-Langevin, Grenoble, France, [5] University of Edinburgh, School of Geosciences, Edinburgh, United Kingdom, [6] Paul Scherrer Institute, ICON, Villigen, Switzerland, [7] University Grenoble Alpes, ISTER, University Savoie Mont Blanc, CNRS, IRD, IFFSTTAR, ISTerre, Grenoble, France

Understanding fluid flow in rocks is crucial to quantify many natural processes such as ground water flow and naturally triggered seismicity, as well as engineering questions such as displacement of contaminants, the eligibility of subsurface waste storage, geothermal energy usage, oil and gas recovery and artificially induced seismicity. Two key parameters that control the variability of fluid flow and the movement of dissolved chemical species are (i) the local hydraulic conductivity, and (ii) the local sorption properties of the dissolved chemical species by the solid matrix. These parameters can be constrained through tomography imaging of rock samples subjected to fluid injection under constrained flow rate and pressure. The neutron imaging technique is ideal to explore fluid localization in porous materials due to the high but variable sensitivity of neutrons to the different hydrogen isotopes. However, until recently, this technique was underused in geology because of its large acquisition time. With the improved acquisition times of newly set-up neutron beamlines, it has become easier to study fluid flow. In the current set of experiments, we demonstrate the feasibility of *in-situ* 2D and 3D time-lapse neutron imaging of fluid and pollutant percolation in rocks, in particular that of cadmium salt. Cadmium is a hazardous compound that is found in many electronic devices, including batteries and is a common contaminant in soil and groundwater. It also exhibits higher contrast in neutron attenuation with respect to heavy water, and is therefore an ideal tracer. Time-lapse 2D radiographies and 3D neutron tomographies of the samples were acquired on two neutron beamlines (ILL, France and SINQ, Switzerland). We performed two sets of experiments, imbibition and injection experiments, where we imaged *in-situ* flow properties, such as local permeability and interactions between cadmium and the solid rock matrix. Our results indicate that even within these cm-scale porous rocks, cadmium transport follows preferential pathways, and locally interacts within the limestone samples. Our results demonstrate that the use of neutron imaging provides additional insights on subsurface transport of pollutants.

Keywords: neutron imaging, cadmium, porous rocks, pollutant transport, sorption, advection

OPEN ACCESS

Edited by:
Lucia Mancini, Elettra Sincrotrone Trieste, Italy

Reviewed by:
Burkhard Schillinger, Technical University of Munich, Germany
Branko Bijeljic, Imperial College London, United Kingdom

****Correspondence:***
Benoît Cordonnier
cordonnier.benoit@gmail.com

Specialty section:
This article was submitted to Earth and Planetary Materials, a section of the journal Frontiers in Earth Science

Received: *21 June 2019*
Accepted: *04 November 2019*
Published: *26 November 2019*

Citation:
Cordonnier B, Pluymakers A, Tengattini A, Marti S, Kaestner A, Fusseis F and Renard F (2019) Neutron Imaging of Cadmium Sorption and Transport in Porous Rocks. Front. Earth Sci. 7:306. doi: 10.3389/feart.2019.00306

1. INTRODUCTION

Historically, laboratory measurements on fluid flow properties through rocks had to rely on data from sensors at the end surfaces of the rock specimen. Such data only yields bulk flow properties and information about spatial heterogeneity or non-linearity of flow within the sample is not accessible. Additionally uncertainties linked with these circuitous observations force researchers to recursively confirm the experiments before stating potential causality. These limitations of the classical approach have pushed experimental geologists toward new *in-situ* measurements techniques. Recent advances in tomographic measurements, specifically, X-rays, neutrons and magnetic resonance imaging techniques, allow a more detailed observation of the rock internal structure and its evolution through time (Carlson, 2006). Additionally, 3D image analysis, such as Digital Volume Correlation (DVC), provides local strain tensors showing localization and strain distribution within the specimens (Viggiani et al., 2007; Tudisco et al., 2015, 2019; Macente et al., 2018). Among the different approaches to obtain 3D tomograms, X-ray imaging is traditionally preferred over neutron as it allows higher spatial and temporal resolution (Pacureanu et al., 2012; Cnudde and Boone, 2013; Olbinado and Rack, 2019). Additionally, the recent increase in number of X-ray computed tomography desktop facilities in universities and research institutes has made X-ray imaging more accessible. As a consequence, this technique is becoming more and more widespread in the geoscience community (Desrues et al., 2006 and references therein). X-rays interact with the atom's electronic cloud while neutrons interact with the atom's nuclei, providing alternative attenuation and diffraction spectra. It results in that, compared to X-rays, neutrons allow imaging of alternative elements with high properties of absorption (e.g., metals) or scattering (e.g., hydrogen). Since hydrogen, present in most geological fluids, strongly attenuates neutrons, neutron imaging is ideal to study rocks with small fluid fractions (i.e., low porosity, Lanza et al., 1991). Neutron imaging in geomaterials historically started more than 20 years ago and from the very beginning focused on flow in porous media (Jasti et al., 1987; Lanza et al., 1991; Degueldre et al., 1996). One of the main interests has been put on imbibition tests, performed either with time-lapse 2D radiography or 3D tomography (Masschaele et al., 2004; Middleton et al., 2005; Carminati et al., 2007; Cnudde et al., 2008; Hall et al., 2010; Zhang et al., 2010; Trtik et al., 2011; Sedighi-Gilani et al., 2012; Derluyn et al., 2013; Kang et al., 2013; Cheng et al., 2015; DiStefano et al., 2017). Additional geologically relevant fields were investigated such as deformed and cracked samples (Hall, 2013; Tudisco et al., 2015, 2019), drying concrete (De Beer et al., 2004; Poulikakos et al., 2013; Toropovs et al., 2015; Dauti et al., 2018) or fossils (Dawson et al., 2014). However, to date, following dynamic processes in 3D time series has remained scarce due to long acquisition times of most neutron facilities. Moreover, experimental devices that allow studying rock samples under confining pressures, i.e., geologically relevant conditions, were rare (Yehya et al., 2018). Recent developments in neutron tomography techniques now allow for faster tomography and enable scientists to capture fluid and contaminant flow at high spatial and temporal resolution (Masschaele et al., 2004; Kaestner et al., 2007, 2016; Lehmann et al., 2007; Tötzke et al., 2011; Tremsin et al., 2011; Tudisco et al., 2019). In our study, we present an experimental set-up which can study fluid flow and cadmium contaminant flow through porous rocks under confining pressures (Pc) relevant to shallow subsurface aquifers (Pc=1 MPa).

Pollution of soil and ground-water is a serious health threat where heavy metals express one of the highest hazards. Cadmium (Cd) is a resilient heavy metal which is among the top six pollutants worldwide. It is used in many electronic devices, including batteries. Its unique toxicological profile makes it dangerous also at low concentrations (Satarug and Moore, 2004; Shen et al., 2019). It affects brain cells, lungs and is strongly carcinogenic (Waalkes, 2003; Bertin and Averbeck, 2006; Subramanian and Govindan, 2007). With high rates of transfer from soils to plants (Das et al., 1997; Benavides et al., 2005) compared to other "non-essential elements" (e.g., lead or mercury), cadmium easily accumulates in all biological forms as it is hardly affected by metabolic degradation (An et al., 2001; Satarug et al., 2003; Joseph, 2009; Jiang et al., 2010; Sari and Tuzen, 2014). It is thus a persistent and ubiquitous health risk. Sources of cadmium can be both geogenic or anthropic with hydrological or aeolian transport. Metal fractionation may lead to relatively natural high concentration of Cd in soils and rocks (i.e., limestones) while electronic waste, smelting, metal extraction and tanneries are the main anthropogenic sources (Fishbein, 1981).

Heavy metal transfer and transport occur in all rocks, and the specific properties depend on the rocks' physical and geochemical properties. Soils can be both an accumulating source and buffer for heavy metals or a simple inert porous media. Soils able to accumulate heavy metals may be used as a natural sorbent to treat and prevent pollution from industrial waste effluents (Ghazy et al., 2008; Sari and Tuzen, 2014). If bio-sorbents are also considered, natural rocks offer a strong potential in storing cadmium. Among them phyllosilicates like smectite (bentonite, montmorillonite) (Barbier et al., 2000; Papini et al., 2004; Sneddon et al., 2006; Bhattacharyya and Gupta, 2007; El Mouzdahir et al., 2007; Karapinar and Donat, 2009; Kuo and Lin, 2009; Vázquez et al., 2009) or sepiolite (Kocaoba, 2009) are used. Furthermore, limestones are also identified as common sorbent for heavy metals and particularly were used to mitigate cadmium pollution (Rangel-Porras et al., 2010). By comparing common sandstones (which likely will act as inert porous medium) with limestones (capable of sorbing cadmium), one may discriminate if the mechanisms of cadmium retention are to be linked to the differences in porous network characteristics or to chemical and mineralogical properties.

Therefore, understanding and quantifying the retention and sorption mechanisms of cadmium in rocks is of tremendous importance for both risk prediction and hazardous waste treatment. Common experimental strategies include tests with various environmental conditions strongly influencing the sorption mechanisms such as flow rate, pH, initial pollutant concentration, or rock composition (Joseph et al., 2019). Here we present results of *in-situ* neutron imaging of flow experiments (imbibition and injection) in limestone and sandstone samples.

We used Indiana limestone and Fontainebleau-, Eselfuhrter-, and Bentheim sandstones, which are all porous sedimentary rocks considered to be homogeneous on the centimeter-scale. We rather used heavy than common water for the lower neutron attenuation of deuterium compared to protium. Taking two of the most classic experimental approaches, namely imbibition tests as well as fluid injection, we determined the potential of neutron imaging to improve our understanding of cadmium interaction mechanisms in confined rocks. For the injection experiments we first saturated the samples with heavy water before introducing cadmium (dissolved in heavy water) within the system, and subsequently rewashed the samples with heavy water. We explored the potential and limits of *in-situ* neutron imaging in porous rocks in the presence of cadmium. Strongly interacting with neutrons, cadmium brings all the potential of neutron imaging. Our experimental set-up (**Figure 1**) confines the samples to a few MPa and thus reproduces the flow of pollutant in rocks at a few tens of meters depth.

2. METHODS

Experiments were performed on three different sandstones (Eselfuhrter, Bentheim, Fontainebleau) and one limestone (Indiana). The cylindrical samples were prepared by coring rock blocks perpendicularly to the sedimentary layering with water cooled diamond drill bits, and rectifying the upper and lower surface of the cylinders to ensure parallelism. The Eselfuhrter sandstone (ES), Bentheim sandstone (BS) and Fontainebleau Sandstone (FS) hold a porosity fraction of 0.21, 0.25, and 0.07 ($\pm$0.03), respectively (Peksa et al., 2015; Barnhoorn et al., 2018). The Indiana limestone (IL) has been measured with a He-pycnometer to a porosity fraction of 0.16 (Barnhoorn et al., 2018).

For all samples, pore fraction was in the range 0.15–0.25. Therefore, when the neutron beam traverses a sample with a diameter of 5 cm, 7.5–12.5 mm of the path will occur through the water phase in the center of the sample when full fluid saturation of the sample is attained. To optimize the signal to noise ratio we ensured that the fluid used would neither be too transparent, neither too opaque to neutrons but used a reasonable portion of the sensor dynamic range. A series of calibration have been performed to identify the most suitable fluids for the injection (**Figure 2**). We successively filled 8 mm inner diameter aluminum crucibles with H_2O, D_2O (deuterium heavy water) and solutions of either H_2O or D_2O with cadmium under concentrations of 0.05 and 0.5 mol/L. The cadmium solution was prepared by dissolving a $CdCl_2$ salt into D_2O. Taking into account the relatively high porosity of the rock samples, the sample size and relative neutron absorptions properties of all the components of the experimental set-up, the optimal dynamic range for the acquired image was obtained when using deuterium water (see **Figure 2** and caption for further details).

Series of flow-through experiments have been performed at two different neutron sources: the D50 beamline (Tengattini et al., 2017) of the Institut Laue-Langevin (Grenoble, France) and the ICON beamline of SINQ (Kaestner et al., 2011a) at the Paul Scherrer Institut (Villigen, Switzerland). The first one is a fission type source where neutron flux can be as high as 1.5 10^{15} n/cm^2/s, while the second one is a spallation type source with a flux as high as 10^{14} n/cm^2/s. During our experiment time, the ILL nuclear core was only at half of its optimal flux, thus bringing it closer to the flux values of SINQ. Imbibition tests were performed at ILL, the injection ones at PSI.

In order to complete the fluid injection experiments, three experimental core holders have been developed. Two were made of ALAA5083, an aluminum alloy known for its low neutron activation and high transparency with neutrons, and Teflon pistons. The third core holder was built with grade 2 titanium, also transparent to neutrons. Having three separate core holders allowed an efficient management of the experimental time as

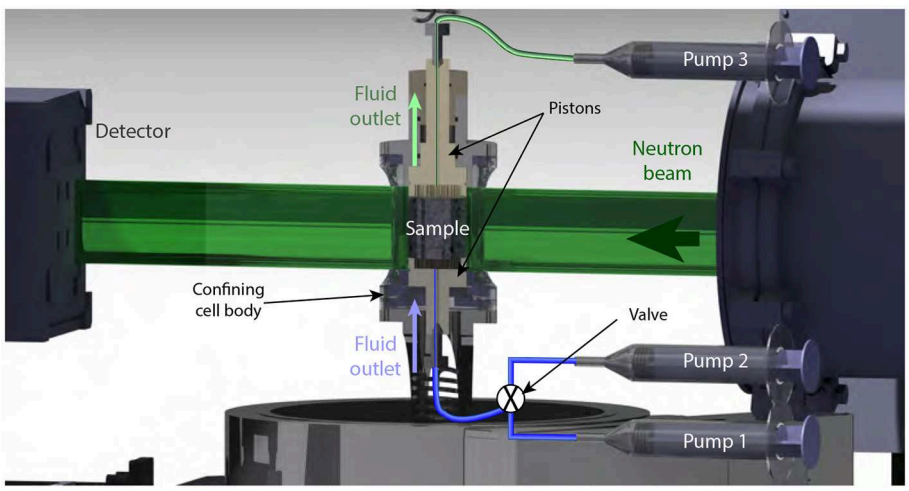

FIGURE 1 | Experimental set-up. A core holder pressurized with nitrogen gas is placed on the rotary stage of the neutron beamline. The sample in the autoclaveA is filled from its bottom side by using one of the two injection pumps. The fluid is recovered by the third pump connected to the top of the sample.

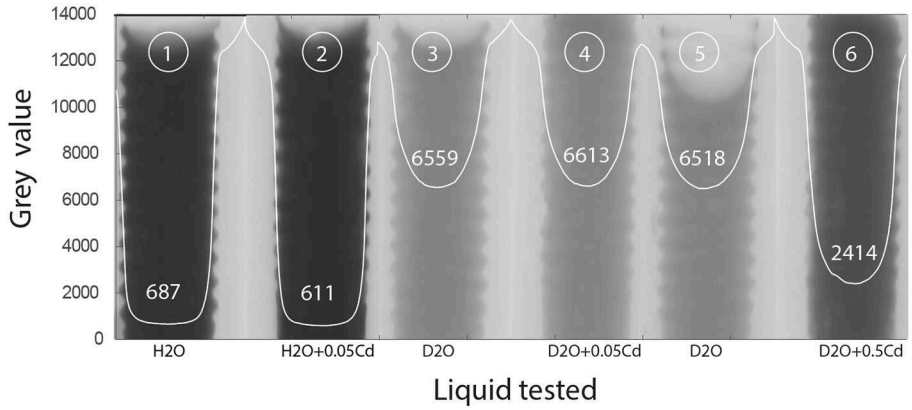

FIGURE 2 | Radiographies and attenuation of injected fluids with, from left to right: (1) H_2O, (2) solution of H_2O with 0.05 mol/L cadmium, (3) D_2O, (4) solution of H_2O with 0.05 mol/L cadmium, (5) D_2O, and (6) solution of H_2O with 0.5 mol/L cadmium. Fluids are placed into 8 mm diameter aluminum crucibles (light gray). Protium based water (1) is attenuating too much and lowers our image projection dynamic range while adding only 0.05 mol/L cadmium to the solution does not give enough contrast (2,4) and falls into the detection method error bar. Hence we ran the experiment with deuterium based water and 0.5 mol/L cadmium concentration (5,6) which are the optimized fluids for the image acquisition of our sample characteristics and optical set-up.

TABLE 1 | List of experiments and experimental conditions.

Experiment number	Experiment name	Sample	Scan type	# proj	Exp. time [s]	Binning	av.	t.d.	ac. time [s]	# volumes	Duration [ml/h]	Flow rate	Liquid
1 (ILL)	Eselfuhrter sandstone	ES01	TomoF	650	0.03	4	3	0	58.5	15	877.5	15	Imbibition test
2 (ILL)	Bentheim Sandstone	BS01	TomoF	900	0.03	4	3	0	81	18	1458	15	Imbibition test
3 (ILL)	Indiana Limestone	IL01	Radio	5548									Imbibition test
4 (ILL)	Indiana Limestone	IL01	Tomo	1599									
5 (SINQ)	Indiana Limestone	IL03	Radio	3145	10	1	1	3.8	43401		0	8	Injection D_2O; Injection D_2O +Cd; Washing D_2O; reinjection D_2O+Cd
6 (SINQ)	Indiana Limestone	IL03	Tomo	627	10	1	1	3.8	8652.6	2	17305.2	0	After D_2O injection, After D_2O +Cd reinjection
7 (SINQ)	Fontainebleau Sandstone	FB02	Radio	2360	10	1	1	3.8	32568			3	Injection D_2O; Injection D_2O+Cd; Washing D_2O
8 (SINQ)	Fontainebleau Sandstone	FB02	Tomo	626	10	1	1	3.8	8638.8	1		1	After D_2O+Cd reinjection

The neutron source used is indicated with the number of each experiment. Scan types are: fast time-lapse 3D tomography (TomoF), high resolution 3D tomography (Tomo), and time-lapse 2D radiography acquisitions (Radio). The averaged frame (av.), time delay between each acquisition (t.d.) and the average acquisition time in seconds (ac. time) are also provided.

one experiment may be prepared while another was running. Additionally, although the rigs were designed for low activation (i.e., low radioactivity level after exposure to neutrons), they still required a so-called radioactive cooling time after each experiment, before being handled at radioactivity levels below the recommended safety limit. All of the cells were composed of a confining cell pressurized to 1 MPa, using nitrogen as a confining medium. The combined use of pressurized gas as a confining medium and neutrons, to our knowledge, for the first time, allows a more transparent apparatus compared to fluid based pressurized cells. The cell had a volume of 240 cm^3 and hosted a 5 by 5 cm cylindrical sample. Two pistons with centered capillary holes on top and bottom of the cylindrical sample allowed fluid circulation (**Figure 1**). Three syringe pumps (Aladdin AL-1000HP) were used, two at the inlet and one at the outlet, allowing the separate injection of two different fluids during the experiments. A given flow rate was imposed on the inlet pump whereas the outlet pump was controlled with a fixed pressure (0.1 MPa). Samples were isolated from the confining medium via Fluorinated Ethylene Propylene (FEP) jackets. After pressurizing the cell, the nitrogen bottle was closed and left at rest for an hour to verify for pressure drops and presence of leaks.

All experiments and experimental conditions are listed in **Table 1**. At the ILL beamline, we performed imbibition tests on initially dry Eselfuhrter and Bentheim sandstones with fast scan tomography where 15 and 18 time-lapse neutron 3D tomography volumes were acquired, respectively (**Table 1**, exp. 1 and 2). Tests consisted in placing the samples in Petri dishes filled with D_2O. Progression of the imbibition front was then imaged by setting the camera in a 4 × 4 binning mode and an exposure time of 0.03 s. Each projection (512 × 512 pixels) was calculated by averaging of three 2D radiographs. For both samples, 650 and

900 projections were acquired, respectively, while the sample was rotated over 360 degrees, resulting in a total acquisition time of 1 min and 1 min 20 s for each volume. Reconstructed volumes, cropped to the Region Of Interest (ROI), resulted in 300 × 300 × 250 voxels with a resolution of 1700 μm. A supplementary imbibition test has been performed on Indiana limestone but this time with time-lapse 2D radiography to be able to follow rapid changes within the sample (**Table 1**, exp. 3). Prior to this test, a full tomography of the IL sample before experiment has been performed (**Table 1**, exp. 3) which provided information on its 3D structure.

For the injection experiments at the ICON beam line (PSI, Switzerland) samples were placed in the apparatus and pressurized at 1 MPa confining pressure with a nitrogen bottle. Two pore volumes of D_2O were first injected for both one Fontainebleau sample and one Indiana sample at a flow rate of 3 and 8 mL/h, respectively. Then, two pore volumes of D_2O+Cd were injected at similar flow rates. We then "washed" the sample by injecting again two pores volumes of D_2O. In the case of the Indiana limestone sample a second injection of the cadmium solution was performed for comparison with the first injection. Two series of radiographs acquisitions were successively performed on both samples (**Table 1**, exp. 5 and 7). Additionally, three 3D tomographies were acquired; two on the Indiana limestone sample after the injection of D_2O and D_2O+Cd (**Table 1**, exp. 6), and one on Fontainebleau sandstone after the injection of D_2O+Cd (**Table 1**, exp. 8). For both radiography and tomography acquisitions, the exposure time was 10 s with no binning nor averaging of projections and a delay of 3.8 s. between each acquisition. Each projection was acquired with a size of 2160 × 2560 pixels and each tomography was composed of 625 projections acquired over a rotation of 180 degrees, leading to a resolution of 250 μm. Unfortunately, several failures of the camera controlling computer led to several hiatuses in the time series, but trends over time could still be followed.

Once the acquisition was performed, radiography raw images were enhanced as follows: (1) First, flat field correction was performed to remove the source contribution and extract only the attenuation of the sample. Beer-Lambert relation was applied on the raw images by normalizing with the bright and dark field references. (2) A second normalization was performed with the initial image averaged over a minimum of 10 projections. With these operations, most of the signal coming from the rock could be removed, enhancing the signal from the injected fluid. (3) The common logarithm of the resulting image was then weighted and divided by the sample thickness at each point of the projection to correct for the variable neutron path length in a cylindrical sample. We used the assumption that samples are perfect cylinders, so thickness was estimated using the cylinder axis and the position of the edges was determined from the overall attenuation of the sample. Up to these three steps, the operations are summarized in Equations (1, 4) Last, for time curve plots each image was averaged and reduced to a 13x13 pixels image. Local averages allowed smoothing heterogeneous effects of the sample while keeping the general trend of the flow for each region.

Summing up the first three steps leads to:

$$ImFin_{i,j} = \frac{log\left(\frac{ImRaw_{i,j} - DF_{i,j}}{BF_{i,j} - DF_{i,j}}\right)}{2\left(R^2 - r_{i,j}^2\right)^{\frac{1}{2}}} \quad (1)$$

where *ImFin* is the resulting image, *ImRaw* the raw original image, *DF* is the dark field image reference, *BF* is the bright field image reference, *R* is the radius of the sample and $r_{i,j}$ is the pixel radius from the center of sample at the given coordinates *i* and *j*.

3. RESULTS

Imbibition tests of Indiana limestone and Eselfuhrter and Fontainebleau sandstones exhibited relatively short flooding times of 45, 15, and 10 min, respectively, corresponding to flow rates between 10 to 150 ml/h. These numbers evidence the variability of the permeability of the samples. Imbibition tests have been widely used in previous studies as a first characterization of the samples (**Figure 3**). Semi-analytical solutions and experimental results demonstrated that the front progression is known to scale with the square root of time (Middleton et al., 2005; Kang et al., 2013; Cheng et al., 2015; DiStefano et al., 2017). From the saturation index of the sample, capillary pressures may be estimated vs. the sample saturation and a relative permeability calculated (Li and Horne, 2005; Haugen et al., 2014; Alyafei and Blunt, 2016, 2018). Complete calculation may be found in Alyafei and Blunt (2018). In the present study, even with a few tomograms, the front progression may easily be estimated. It also linearly scales with the square root

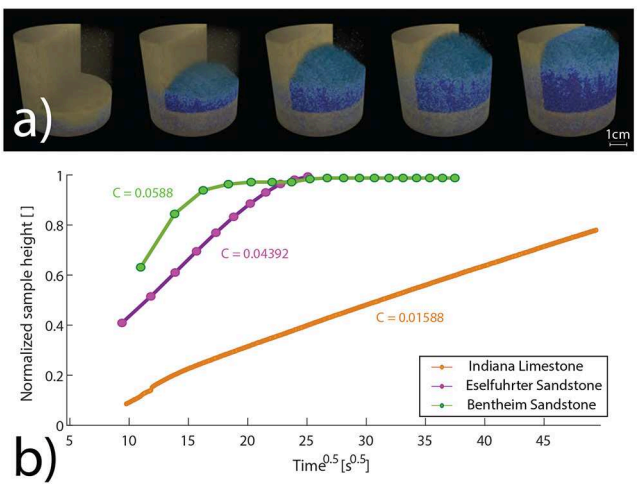

FIGURE 3 | Neutron imaging of the imbibition of porous rocks with D_2O. **(a)** Three-dimensional rendering time series of Eselfuhrter sandstone. The sample has been virtually cropped to evidence the progression of waterfront, represented in blue. **(b)** Progression of the waterfront along the normalized sample height vs. the square root of time for Indiana limestone, Eselfuhrter sandstone and Bentheim sandstone. The slope of the front progression defines the commonly called "sorptivity" constant, here marked as C.

of time and from the slope calculated we may easily sort the Indiana limestone, the Eselfuhrter sandstone and the Fontainebleau sandstone samples as having an increasing relative permeability.

From the results of the injection experiments at the ICON beamline, we observed the evolution, dispersion and alteration of the cadmium concentration from the two different injected fluids into the Indiana limestone and Fontainebleau sandstone. Assuming that the linear attenuation coefficients of cadmium and deuterium are constant through time, we can use the Beer-Lambert law to estimate the cadmium concentration and its relative evolution with time. Note however that our method, based on the data from the dry samples, remains simplified. A more elaborated approach would first attempt reducing the polychromatism of the neutron beam in order to correct the beam hardening effect and so the intensity profile on the sides of the sample. Then another correction would be on the scattering of the sample with and without fluid but also the background scattering (Boillat et al., 2018; Carminati et al., 2019). Such a correction would reduce the cupping effect generated by scattered neutrons. Cupping and beam hardening effects induce some bias on the data from the radial sides of our samples and so only the central region of the sample was used in the analysis. Finally, a further correction must be made to account for the fluid thickness crossed at each point of the radiography. This implies that a true quantification of the cadmium concentration requires performing these experiments with a full tomographic time series to obtain the knowledge of the pore thickness at each point of the projection. This could be achieved by performing prior to the experiment a registered tomography or acquiring a few projections at different angles during the experiment. A third approach could be a mixture of the two with the method of the golden ratio (Kaestner et al., 2011b; Wang et al., 2017). Nevertheless, the image processing as presented here [see Equation (1)] provides a general trend to estimate the cadmium concentration.

In **Figure 4** are presented The two radio-projection time series of both Fontainebleau sandstone (**Figure 4A**) and Indiana limestone (**Figure 4B**). In **Figure 4A**, the first two lines, slides 1 to 6, display the injection of D_2O, while slides 7 to 9 show the injection of D_2O+Cd. Note that during the first D_2O injection, the water front is slightly brighter, which may be due to some cadmium left over into the injecting tube from previous experiments. The last three slides visualize the washing phase with injection of D_2O. One may note that slides 6 and 12, both final stages of the D_2O injection, are extremely comparable and this suggests that most of the cadmium has been removed during this washing phase. In **Figure 4B**, slides 1 to 5 display the injection of D_2O, slides 6 to 8 show the injection of D_2O+Cd and slides 9 to 11 display the washing phase. We may observe numerous bright spots remaining after the washing phase, suggesting that some Cd remained trapped in the sample. Slide 12 is the onset of the new D_2O+Cd injection. **Figure 5** shows, for each injection experiment in the Fontainebleau sandstone and Indiana limestone, the time evolution of cadmium at different locations of the sample. From the 13 × 13 pixels averaged images we selected a grid covering the central area of the sample (see **Figure 5**). Distinct vertical sections of the sample are presented with different colors. Different radial positions are presented with different color saturations. The center of the sample is displayed with thicker curves. From these data, a vertical gradient, almost linear, is observed across the height of the sample. This linear trend may be interpreted as a lower water saturation and concentration of cadmium at the top of the sample compared to the bottom part once the fluid and pollutant were injected. This is in stark contrast with the Fontainebleau sandstone, which does not display any significant horizontal gradient (the cadmium concentration on the sides of

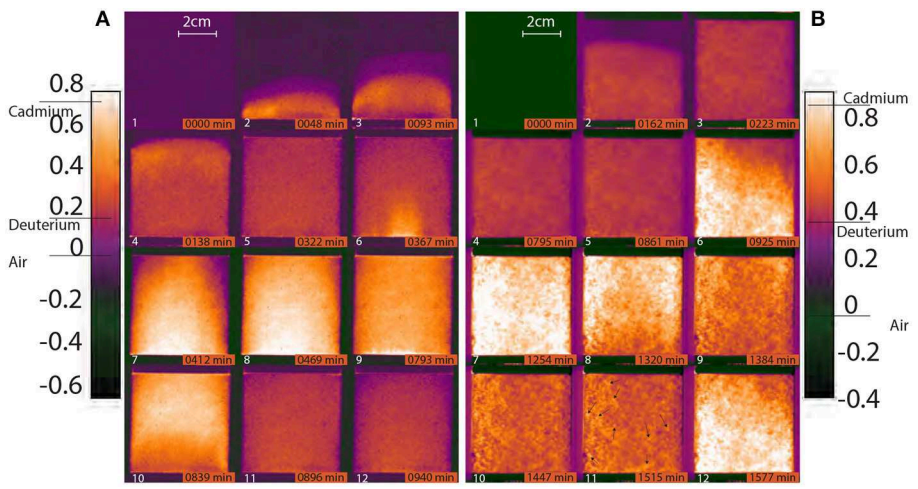

FIGURE 4 | Time-lapse 2D radiographs of injection of cadmium in **(A)** Fontainebleau sandstone and **(B)** Indiana limestone. The first injection of D_2O was followed by an injection of D_2O +Cd. Samples were then washed with a second injection of D_2O. For the limestone only, a second injection of D_2O+Cd has been performed at the end of the experiment. The color code shows the range expected for air, D_2O, and D_2O+Cd. Black arrows in slide 11, **(B)**, evidence the spots where "unwashed" cadmium is maximum. Note, however, that comparing slide 11 and 5, most of the sample contains some unwashed cadmium.

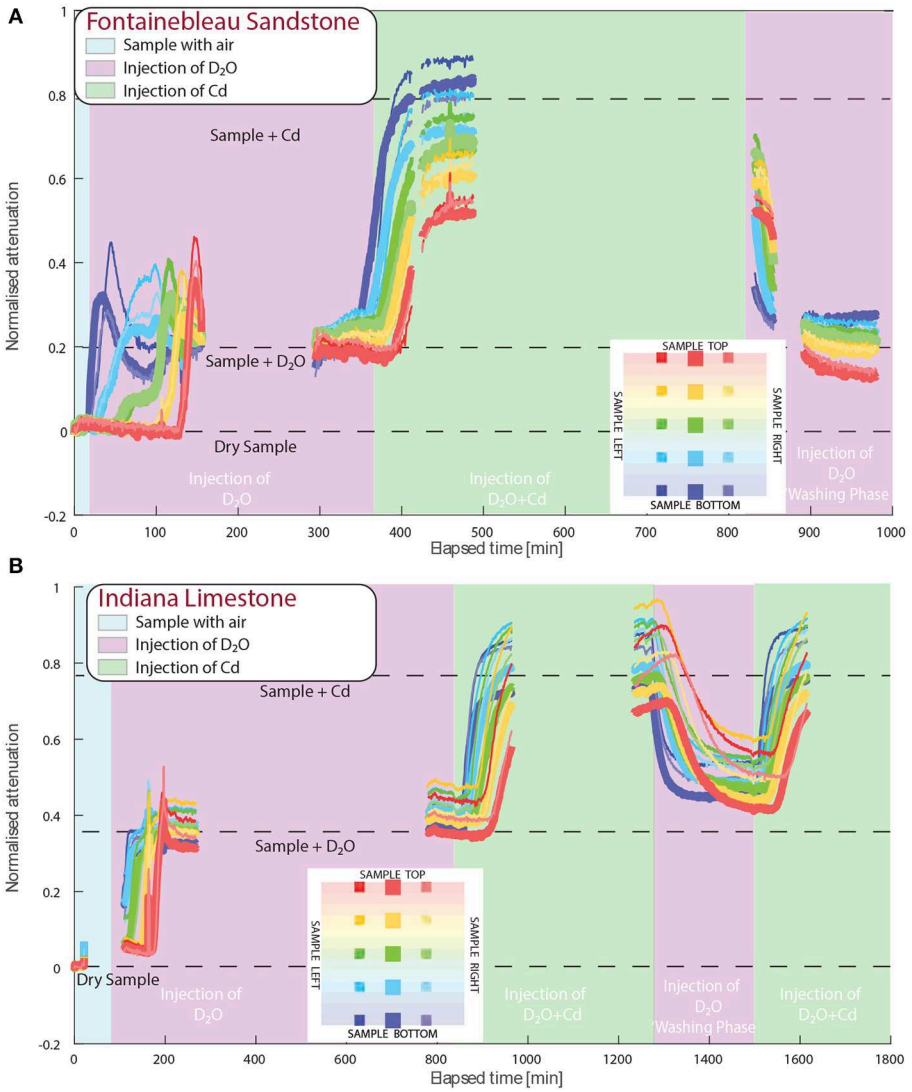

FIGURE 5 | Normalized neutron attenuation in the samples vs. time. Hiatuses in the data correspond to failures of the camera system or tomography acquisition. The different curves display different regions in the sample, as mapped in the figure inset. The central region of the sample has an increased thickness for easier visualization. **(A)** Fontainebleau sandstone experiment. The first injection of D_2O shows a slight overshoot before 200 min. due to some left-over cadmium from the previous experiment still present in the tubing system. **(B)** Indiana limestone experiment.

the samples nearly superimposes the curves from the center of the sample). Conversely, the Indiana limestone sample displays a horizontal gradient from the left to right side. Even though the limestone and sandstone samples display overall very similar behaviors, careful observation indicates that only for limestone, the cadmium is not completely removed during the D_2O washing phase as the curves do not come back to their initial values (**Figure 5B**). By normalizing the curve drop during the washing phase with the stable values of D_2O+Cd and D_2O during the first and second injection phases, one may measure how much of the cadmium was removed during the washing phase. The curve drop during the washing phase evidences that about 60% of the total cadmium is quickly removed and then stabilizes to a value of 70%, indicating that 30% of the injected cadmium is still present in the sample. On the other side, in less than 200 min of D_2O injection, the Fontainebleau sandstone recovered the original D_2O value and we conclude that the sample has been fully washed and all the pollutant flushed out. Within the Indiana limestone, local areas are seen to have captured and preserved the cadmium. They appear as brighter spots, on **Figure 4** highlighted by arrows on slide 11, section b. Further analyses on these specific areas have been performed and revealed that these locations retained 42 to 55 % of the cadmium originally injected with an average of 48±4% (standard deviation), see arrows in **Figure 4**. Note however that the projections of these spots are influenced by the material in front and behind them. Despite picking the darkest areas where the sample is the thinnest and less influenced, this estimation represents a lower bound

on the amount of trapped cadmium. For the same reasons, these cadmium locations were mostly visible on the sides of the samples where they were less affected by cleaned (i.e., Cd-free) rock material. Nevertheless one side of the sample remained predominantly contaminated (see **Figure 4**). This is also reflected by the preferential infiltration of both the D_2O and D_2O + Cd injection front (**Figure 4B**). This observation indicates that even for this Indiana limestone, usually considered to be a relatively homogeneous medium in terms of composition and grain size at the scale of laboratory samples, a variation of permeability is present within the sample. Such heterogeneities can not be observed by conventional flow-through tests. Previous experiment did not evidence any pronounced tailing on Indiana limestone (Gist et al., 1990) but numerical simulations already evidenced a large range of fluid velocities (Bijeljic et al., 2013). Our results therefore present the first evidence of *in-situ* non-Fickian transport of pollutants in porous rocks.

4. DISCUSSION

Solute transport is normally described by advection dispersion equations. The plume of a pollutant through porous media can consequently be modeled accordingly if one knows the mean velocity of the fluid. When anomalies are observed, transport is then described as non-Fickian (Becker and Shapiro, 2003; Levy and Berkowitz, 2003; Gouze et al., 2008). Sources of non-Fickian behavior may vary, such as fluids trapped or delayed in the pore network or sorption of the pollutant within the host rock. In order to be sorbed in rocks, inorganic pollutants must first move from the bulk solution to the fluid boundary layer within the rock pores and then from the boundary layer to the rock surface. From there, they may adsorb to an active site of the surface, following either a chemical reaction or an exchange of ions with the surface. Eventually, if the surface is sufficiently porous, it will allow these pollutants to diffuse and to be incorporated inside the solid elements of the rock. These four steps will have different efficiencies depending on the flow rate, pH, initial concentration of the pollutant, chemical composition of the rock and the amount of active sorption: sites present. The use of different existing models (e.g., Langmuir model or Freundlich model), which are based on different assumptions, may help determining the sorption mechanisms. The Langmuir model is based on the assumption that the number of sites is limited compared to the amount of solute material. The Freundlich model assumes a greater number of active sites compared to the available solute material. Indiana limestone itself has been identified among other carbonates to be a rock with a wide range of flow velocities (Bijeljic et al., 2013), interpreted to be a result from the bimodal porosity distribution. The throats connecting the pores have been evidenced with two characteristic diameters of 20 and 0.4 μm. The dispersion of the fluid within the porosity connected by thin throats may lead to pockets of slow or stagnant fluids. Finally, diffusion coefficients of cadmium in water may be approximated in the range of $710^{-10} m^2 s^{-1}$ (Lide and Kehiaian, 1994; Furukawa et al., 2007). Hence considering spherical or cylindrical diffusion (i.e., pore or throats), from Indiana limestone network characteristics, cadmium will be diffused to the host rock-fluid interface in much less than an hour. Such pockets may consequently ease the sorption process. At the current stage of our study it is not yet possible of distinguishing if the remaining cadmium has been sorbed or trapped in a stagnant fluid pocket. Further experiments are necessary to determine the mechanisms behind the local interaction of the cadmium with the rock. A post-experimental X-ray tomography acquisition of the Indiana limestone sample, oriented along the projection of the radiography, provides some explanation on the reasons why the permeability and potentially sorption were higher on the sides of the sample. In **Figure 6**, one may observe a vertically heterogeneous layering. On the left side, several large pores and fragments of marine organisms are present. On the right side a similar composition but with lower pore size, is observed. Indiana limestone is known for being a homogeneous and quasi exclusively calcite limestone (Handin et al., 1971; Barnhoorn et al., 2018). In between the rock matrix, the fragments appear to be less attenuating either due to a different composition or a lower density. Hence, we propose that the differences in attenuation are due to the density variations of the background rock matrix and pore network. This effect could be explained by some of the large marine fragments that were crushed, filling the large pores and creating microporosity in between the fragments. Overall, the total pore

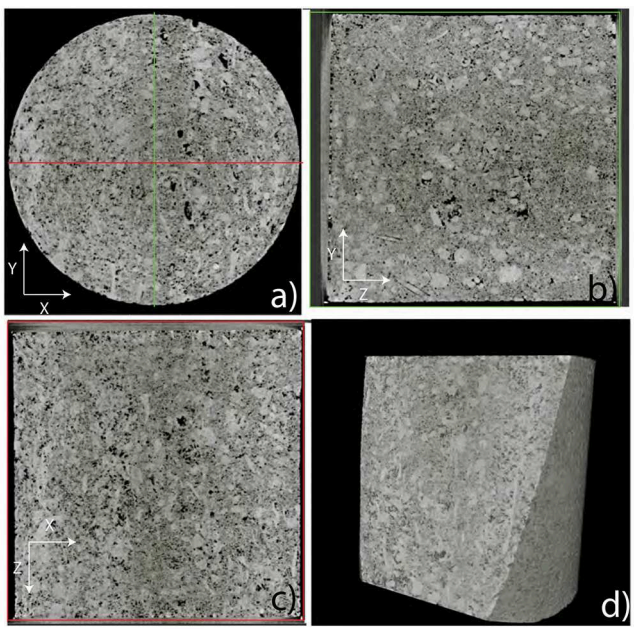

FIGURE 6 | X-ray tomography of the Indiana limestone sample IL3 (exp. 5). The sample is a cylinder with dimensions of 5 × 5 cm. **(a)** Slice in the middle of the sample, top view. **(b)** Slice in the middle of the sample, right side view. **(c)** Slice in the middle of the sample, front view. **(d)** 3D volume rendering. The pores in the sample are represented in black while fossil and sediment fragments are represented in bright or light gray. A darker gray domain, mostly in the center of the sample corresponds to lower density, fossil fragments are difficult to distinguish. They probably corresponds to fragments reduced into powder with consequently a higher inner porosity than the intact fragments.

fraction throughout the sample may not have changed but the polydispersity of the poresize distribution has been modified. The mixture of fragments with small pores is shown in **Figure 6** with lower gray values as their overall density is lower than the density of the intact fragments. It would offer a bimodal permeability, distinguishing the main flow from smaller pockets where the fluid would be delayed or approximated as stagnant over the experimental time-scale. It would make these sites ideal for cadmium sorption within the host rock. This shows that sample-scale sorption experiments, such as been performed in the past on dolomitic and calcitic limestones, can therefore be significantly improved with *in-situ* imaging, which can take into account the small-scale heterogeneities that affect flow and sorption. Neutron imaging, with its remarkable sensitivity to fluids, has now reached a level of technicality where fast time-series of tomographies can be acquired. Moreover, the recent advance on the correction of scattering bias has improved the quantitative possibilities of the method (Boillat et al., 2018; Carminati et al., 2019).

5. CONCLUSIONS

With the present study we demonstrated that neutron beamlines are ready for the use of *in-situ* experimental devices with confining pressure that allow to study contaminant transport in rocks. Radiography and tomography time-series can be acquired and image geological processes under earth-like conditions. Using cadmium as a tracer, we investigated the case study of pollutant flow in different porous rocks. Moreover, we have also demonstrated that the use of either protium- or deuterium-based water allows for greater flexibility when choosing sample-type and sample size, with respect to the expected ranges in porosity and permeability. We used a centimetersized sample, which is generally considered to be homogeneous using traditional set-ups for flow experiments. Our neutron tomography experiments indicate that even at this small scale localization of flow and preferential adsorption takes place, indicating non-Fickian transport of the aqueous species. Now the feasibility of neutron usage has been ascertained to study cadmium transport in porous rocks, the next step will be to perform similar experiments with different initial concentrations in order to further understand which mechanisms prevail (retention or sorption), as a function of experimental conditions, space and time. Additionally, further experiments need to be performed with tomography time series in order to better localize the areas where the residual cadmium is maximum and to investigate further these locations. Regardless of improvements of the imaging methods, this study demonstrates that Indiana limestone has a real potential in cadmium retention. It therefore provides a new perception of pollutant capture, where only a fraction of the rock structure contributes to the retention of heavy metal pollutants.

DATA AVAILABILITY STATEMENT

The datasets (2D and 3D neutron data) are available in the public repository NORSTORE (https://doi.org/10.11582/2019.00021, Renard, 2019).

AUTHOR CONTRIBUTIONS

All authors listed have made a substantial, direct and intellectual contribution to the work, and approved it for publication.

FUNDING

This study received funding from the Norwegian Research Council (project ARGUS, grant 272217). AP was currently support by a VENI project, with grant number 016.Veni.181.036, funded by the Dutch Foundation for Scientific Research (NWO).

ACKNOWLEDGMENTS

We thank Auke Barnhoorn at TU Delft for providing several rock samples.

REFERENCES

Alyafei, N., and Blunt, M. J. (2016). The effect of wettability on capillary trapping in carbonates. *Adv. Water Resour.* 90, 36–50. doi: 10.1016/j.advwatres.2016.02.001

Alyafei, N., and Blunt, M. J. (2018). Estimation of relative permeability and capillary pressure from mass imbibition experiments. *Adv. Water Resour.* 115, 88–94. doi: 10.1016/j.advwatres.2018.03.003

An, H. K., Park, B. Y., and Kim, D. S. (2001). Crab shell for the removal of heavy metals from aqueous solution. *Water Res.* 35, 3551–3556. doi: 10.1016/S0043-1354(01)00099-9

Barbier, F., Duc, G., and Petit-Ramel, M. (2000). Adsorption of lead and cadmium ions from aqueous solution to the montmorillonite/water interface. *Colloids Surf. A Phys. Eng. Aspects* 166, 153–159. doi: 10.1016/S0927-7757(99)00501-4

Barnhoorn, A., Douma, L., and Janmahomed, F. (2018). Experimental load cycling in the brittle field produces a more distributed fracture network. *Geophys. Res. Abstr.* 20.

Becker, M. W., and Shapiro, A. M. (2003). Interpreting tracer breakthrough tailing from different forced-gradient tracer experiment configurations in fractured bedrock. *Water Resour. Res.* 39. doi: 10.1029/2001WR001190

Benavides, M. P., Gallego, S. M., and Tomaro, M. L. (2005). Cadmium toxicity in plants. *Braz. J. Plant Physiol.* 17, 21–34. doi: 10.1590/S1677-04202005000100003

Bertin, G. and Averbeck, D. (2006). Cadmium: cellular effects, modifications of biomolecules, modulation of DNA repair and genotoxic consequences (a review). *Biochimie* 88, 1549–1559. doi: 10.1016/j.biochi.2006.10.001

Bhattacharyya, K. G., and Gupta, S. S. (2007). Adsorptive accumulation of Cd(II), Co(II), Cu(II), Pb(II), and Ni(II) from water on montmorillonite: influence of acid activation. *J. Coll. Interface Sci.* 310, 411–424. doi: 10.1016/j.jcis.2007.01.080

Bijeljic, B., Mostaghimi, P., and Blunt, M. J. (2013). Insights into non-fickian solute transport in carbonates. *Water Resour. Res.* 49, 2714–2728. doi: 10.1002/wrcr.20238

Boillat, P., Carminati, C., Schmid, F., Grünzweig, C., Hovind, J., Kaestner, A., et al. (2018). Chasing quantitative biases in neutron imaging with scintillator-camera detectors: a practical method with black body grids. *Optics Express* 26, 15769–15784. doi: 10.1364/OE.26.015769

Carlson, W. D. (2006). Three-dimensional imaging of earth and planetary materials. *Earth Planet. Sci. Lett.* 249, 133–147. doi: 10.1016/j.epsl.2006.06.020

Masschaele, B., Dierick, M., Cnudde, V., Hoorebeke, L., Delputte, S., Gildemeister, A., et al. (2004). High-speed thermal neutron tomography for the visualization of water repellents, consolidants and water uptake in sand and lime stones. *Radiat. Phys. Chem.* 71, 807–808. doi: 10.1016/j.radphyschem.2004.04.102

Middleton, M., Li, K., and de Beer, F. (2005). *Spontaneous Imbibition Studies of Australian Reservoir Rocks With Neutron Radiography*. Irvine, CA: Society of Petroleum Engineers.

Olbinado, M. P., and Rack, A. (2019). "Recent advances on *in situ* materials characterization using ultra high-speed x-ray imaging at The European Synchrotron ESRF," in *32nd International Congress on High-Speed Imaging and Photonics*, eds M. Versluis and E. Stride (Enschede: SPIE), 16.

Pacureanu, A., Langer, M., Boller, E., Tafforeau, P., and Peyrin, F. (2012). Nanoscale imaging of the bone cell network with synchrotron X-ray tomography: optimization of acquisition setup. *Med. Phys.* 39, 2229–2238. doi: 10.1118/1.3697525

Papini, M. P., Saurini, T., Bianchi, A., Majone, M., and Beccari, M. (2004). Modeling the competitive adsorption of Pb, Cu, Cd, and Ni onto a natural heterogeneous sorbent material (Italian "Red Soil"). *Indus. Eng. Chem. Res.* 43, 5032–5041. doi: 10.1117/12.2524607

Peksa, A. E., Wolf, K.-H. A., and Zitha, P. L. (2015). Bentheimer sandstone revisited for experimental purposes. *Marine Petrol. Geol.* 67, 701–719. doi: 10.1016/j.marpetgeo.2015.06.001

Poulikakos, L. D., Sedighi Gilani, M., Derome, D., Jerjen, I., and Vontobel, P. (2013). Time resolved analysis of water drainage in porous asphalt concrete using neutron radiography. *Appl. Radiat. Isotopes* 77, 5–13. doi: 10.1016/j.apradiso.2013.01.040

Rangel-Porras, G., García-Magno, J. B., and González-Muñoz, M. P. (2010). Lead and cadmium immobilization on calcitic limestone materials. *Desalination* 262, 1–10. doi: 10.1016/j.desal.2010.04.043

Renard, F. (2019). *Neutron Imaging of Cadmium Sorption and Transport in Porous Rocks.* [Data set]. Norstore. doi: 10.11582/2019.00021

Sari, A. and Tuzen, M. (2014). Cd(II) adsorption from aqueous solution by raw and modified kaolinite. *Appl. Clay Sci.* 88–89, 63–72. doi: 10.1016/j.clay.2013.12.021

Satarug, S., Baker, J. R., Urbenjapol, S., Haswell-Elkins, M., Reilly, P. E., Williams, D. J., et al. (2003). A global perspective on cadmium pollution and toxicity in non-occupationally exposed population. *Toxicol. Lett.* 137, 65–83. doi: 10.1016/S0378-4274(02)00381-8

Satarug, S., and Moore, M. R. (2004). Adverse health effects of chronic exposure to low-level cadmium in foodstuffs and cigarette smoke. *Environ. Health Perspect.* 112, 1099–1103. doi: 10.1289/ehp.6751

Sedighi-Gilani, M., Griffa, M., Mannes, D., Lehmann, E., Carmeliet, J., and Derome, D. (2012). Visualization and quantification of liquid water transport in softwood by means of neutron radiography. *Int. J. Heat Mass Transfer* 55, 6211–6221. doi: 10.1016/j.ijheatmasstransfer.2012.06.045

Shen, X., Liu, W., Chen, Y., Guo, Y., Gao, M., Chen, W., et al. (2019). Diagnostic significance of metallothionein members in recognizing cadmium exposure in various organs under low-dose exposure. *Chemosphere* 229, 32–40. doi: 10.1016/j.chemosphere.2019.04.192

Sneddon, I., Orueetxebarria, M., Hodson, M., Schofield, P., and Valsami-Jones, E. (2006). Use of bone meal amendments to immobilise Pb, Zn and Cd in soil: a leaching column study. *Environ. Pollut.* 144, 816–825. doi: 10.1016/j.envpol.2006.02.008

Subramanian, J., and Govindan, R. (2007). Lung cancer in never smokers: a review. *J. Clin. Oncol.* 25, 561–570. doi: 10.1200/JCO.2006.06.8015

Tengattini, A., Atkins, D., Giroud, B., Andò, E., Beaucour, J., and Viggiani, G. (2017). "NeXT-Grenoble, a novel facility for Neutron and X-ray Tomography in Grenoble NEXT-Grenoble," in *3rd International Conference on Tomograpgy of Materials and Structures* (Cairns, QLD).

Toropovs, N., Monte, F. L., Wyrzykowski, M., Weber, B., Sahmenko, G., Vontobel, P., et al. (2015). Real-time measurements of temperature, pressure and moisture profiles in High-Performance Concrete exposed to high temperatures during neutron radiography imaging. *Cement Concrete Res.* 68, 166–173. doi: 10.1016/j.cemconres.2014.11.003

Tötzke, C., Manke, I., Hilger, A., Choinka, G., Kardjilov, N., Arlt, T., et al. (2011). Large area high resolution neutron imaging detector for fuel cell research. *J. Power Sour.* 196, 4631–4637. doi: 10.1016/j.jpowsour.2011.01.049

Tremsin, A. S., McPhate, J. B., Vallerga, J. V., Siegmund, O. H. W., Feller, W. B., Lehmann, E., et al. (2011). Improved efficiency of high resolution thermal and cold neutron imaging. *Nuclear Instrum. Methods Phys. Res. A* 628, 415–418. doi: 10.1016/j.nima.2010.07.014

Trtik, P., Münch, B., Weiss, W. J., Kaestner, A., Jerjen, I., Josic, L., et al. (2011). Release of internal curing water from lightweight aggregates in cement paste investigated by neutron and X-ray tomography. *Nuclear Instrum. Methods Phys. Res. A* 651, 244–249. doi: 10.1016/j.nima.2011.02.012

Tudisco, E., Etxegarai, M., Hall, S. A., Charalampidou, E.-M., Couples, G. D., Lewis, H., et al. (2019). Fast 4-d imaging of fluid flow in rock by high-speed neutron tomography. *J. Geophys. Res. Solid Earth* 124, 3557–3569. doi: 10.1029/2018JB016522

Tudisco, E., Hall, S., Charalampidou, E., Kardjilov, N., Hilger, A., and Sone, H. (2015). Full-field measurements of strain localisation in sandstone by neutron tomography and 3D-volumetric digital image correlation. *Phys. Proc.* 69, 509–515. doi: 10.1016/j.phpro.2015.07.072

Vázquez, G., Sonia Freire, M., González-Alvarez, J., and Antorrena, G. (2009). Equilibrium and kinetic modelling of the adsorption of Cd2+ ions onto chestnut shell. *Desalination* 249, 855–860. doi: 10.1016/j.desal.2009.09.007

Viggiani, G., Lenoir, N., Bornert, M., Desrues, J., and Be, P. (2007). Volumetric digital image correlation applied to X-ray microtomography images from triaxial compression tests on argillaceous rock. *Strain* 43, 193–205. doi: 10.1111/j.1475-1305.2007.00348.x

Waalkes, M. (2003). Cadmium carcinogenesis. *Mutat. Res.* 533, 107–120. doi: 10.1016/j.mrfmmm.2003.07.011

Wang, H., Kaestner, A., Zou, Y., Lu, Y., and Guo, Z. (2017). Sparse-view reconstruction of dynamic processes by neutron tomography. *Phys. Proc.* 88, 290–298. doi: 10.1016/j.phpro.2017.06.040

Yehya, M., Andò, E., Dufour, F., and Tengattini, A. (2018). Fluid-flow measurements in low permeability media with high pressure gradients using neutron imaging: application to concrete. *Nuclear Instrum. Methods Phys. Res. A* 890, 35–42. doi: 10.1016/j.nima.2018.02.039

Zhang, P., Wittmann, F. H., Zhao, T. J., Lehmann, E. H., Tian, L., and Vontobel, P. (2010). Observation and quantification of water penetration into Strain Hardening Cement-based Composites (SHCC) with multiple cracks by means of neutron radiography. *Nuclear Instrum. Methods Phys. Res. A* 620, 414–420. doi: 10.1016/j.nima.2010.04.119

Conflict of Interest: The authors declare that the research was conducted in the absence of any commercial or financial relationships that could be construed as a potential conflict of interest.